

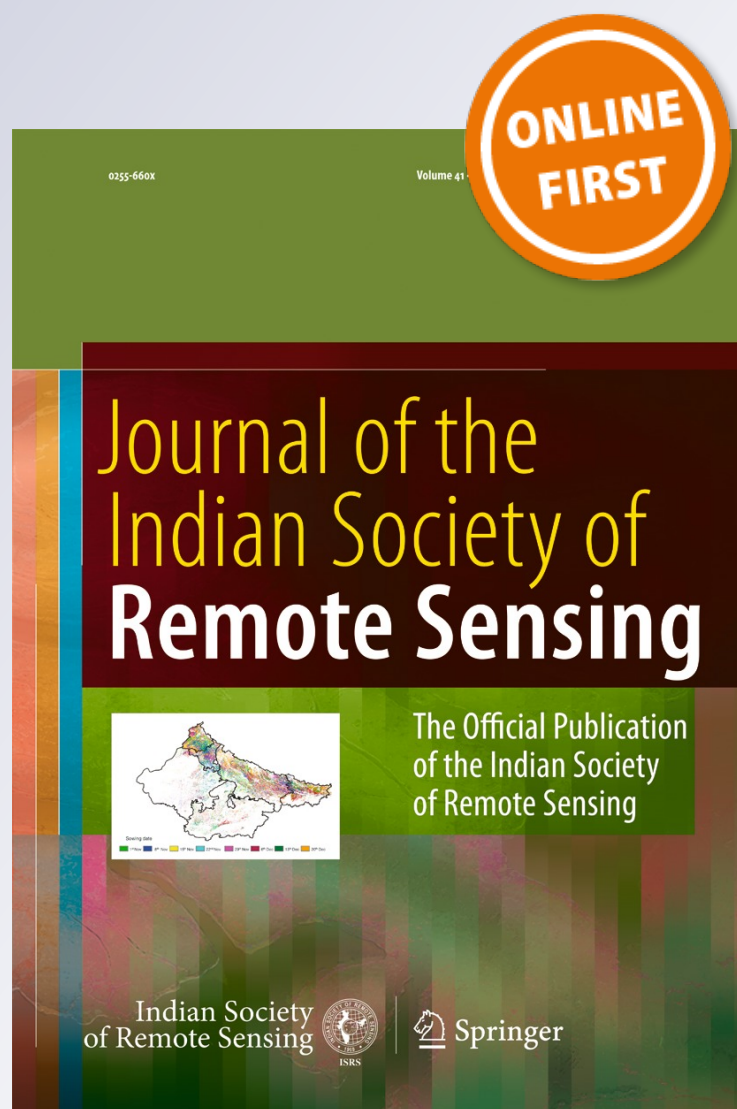
# *DEM Extraction in Urban Areas Using High-Resolution TerraSAR-X Imagery*

**Umut Gunes Sefercik, Naci Yastikli & Iulia Dana**

**Journal of the Indian Society of Remote Sensing**

ISSN 0255-660X

J Indian Soc Remote Sens  
DOI 10.1007/s12524-013-0317-9



**Your article is protected by copyright and all rights are held exclusively by Indian Society of Remote Sensing. This e-offprint is for personal use only and shall not be self-archived in electronic repositories. If you wish to self-archive your article, please use the accepted manuscript version for posting on your own website. You may further deposit the accepted manuscript version in any repository, provided it is only made publicly available 12 months after official publication or later and provided acknowledgement is given to the original source of publication and a link is inserted to the published article on Springer's website. The link must be accompanied by the following text: "The final publication is available at [link.springer.com](http://link.springer.com)".**



# DEM Extraction in Urban Areas Using High-Resolution TerraSAR-X Imagery

Umut Gunes Sefercik · Naci Yastikli · Iulia Dana

Received: 29 December 2012 / Accepted: 12 August 2013  
© Indian Society of Remote Sensing 2013

**Abstract** Three-dimensional (3D) spatial information is crucial for improving the quality of human life through urban planning and management, and it is widely utilized due to its rapid, periodic and inexpensive acquisition. In this context, extraction of digital surface and elevation models (DSM and DEM) is a significant research topic for space-borne optical and synthetic aperture radar (SAR) remote sensing. The DSMs include visible features on the earth's surface such as vegetation, forest and elevated man-made objects, while DEMs contain only the bare ground. In this paper, using TerraSAR-X (TSX) high resolution Spotlight (HS) images, high-resolution interferometric DEM generation in a part of Istanbul urban area is aimed. This is not an easy task because of SAR imaging problems in complex geometry of urban settlements. The interferometric processing steps for DSM generation were discussed including critical parameters and thresholds to improve the quality of the final product and a 3 m gridded DSM was generated. The DSM-DEM conversion was performed by filtering and the quality of generated DEM was verified against a reference DEM from stereo photogrammetry with 3 m original grid spacing. The achieved root mean square error of height differences (RMSZ) varies from 7.09 to 8.11 m, depending on the terrain slope. The differential DEM, illustrates the height differences between generated DEM and the reference DEM, was generated to show the correlation

between height differences and the coherence map. Finally, a perspective view of test area was created draping extracted DEM and a high-resolution IKONOS panchromatic image.

**Keywords** TerraSAR-X · Urban · Interferometric synthetic aperture radar · Digital elevation model · Generation · Accuracy · Perspective view

## Introduction

Three-dimensional (3D) spatial information plays an important role in critical decisions regarding city planning and urban development. Projects that aim to analyze population mobility, road network design, tracking, prevention of illegal housing, etc., in urban areas require accurate digital surface models (DSMs) and digital elevation models (DEMs). DSMs and DEMs are required for a wide range of other applications, such as the creation of perspective views and relief maps (Fraser 2003), orthophoto generation, disaster monitoring and management (Ranganath et al. 2007; Christie et al. 2009; López-Quiroz et al. 2009), geographical information system (GIS) establishment (Jenson and Domingue 1988; Liu et al. 1999; Font et al. 2010), agriculture (Thompson et al. 2001; Schmidt and Persson 2003), forestry (Guindon et al. 1982; Stereńczak and Kozak 2011) and hydrology (Wolock and Price 1994; Jain and Singh 2005). To satisfy this demand, different techniques are employed for DSM and DEM generation. The most preferred techniques are airborne light detection and ranging (LIDAR), photogrammetry, and space-borne remote sensing including stereoscopy using optical or synthetic aperture radar (SAR) imagery (radargrammetry) and SAR interferometry (InSAR). When compared, different space-borne images have different advantages and disadvantages. Object recognition is easier from optical images, but cloud-free coverage is required. Although object recognition is more

U. G. Sefercik (✉)  
Department of Geomatics Engineering, Bulent Ecevit University,  
67100 Zonguldak, Turkey  
e-mail: ugsefercik@hotmail.com

N. Yastikli  
Department of Geomatics Engineering, Yildiz Technical University,  
Davutpasa Campus, 34210 Istanbul, Turkey  
e-mail: ynaci@yildiz.edu.tr

I. Dana  
Romanian Space Agency, Bucharest, Romania  
e-mail: iulia.dana@rosa.ro

difficult from SAR images, data can be collected both day and night regardless of weather conditions.

InSAR has become operational in recent years for DSM generation (Gens and Van Genderen 1996; Herland 1996; Wegmüller et al. 2009) by means of improved ground resolution of up to 1 m with space-borne SAR sensors such as TerraSAR-X (TSX) (DLR 2011) and Cosmo-SkyMed (Cosmo-SkyMed 2011). To use InSAR technique, at least two complex SAR images are required for DSM generation that are either taken simultaneously (single-pass mode) or sequentially (repeat-pass mode) by airborne or space-borne sensors from slightly different viewpoints focused on the same area of interest (Toutin and Gray 2000; Rosen et al. 2000; Hensley et al. 2001; Crosetto 2002). Utilizing single-pass interferometry, the Shuttle Radar Topography Mission (SRTM) generated comprehensive topographic data for mapping near-global landmass (Rabus et al. 2003; Sefercik and Jacobsen 2006, 2007; Yastikli et al. 2006; Sefercik and Alkan 2009). The repeat-pass InSAR technique has been employed in several satellite systems such as ENVISAT, ERS 1–2, RADARSAT 1–2, ALOS, and JERS-1.

Areas settled by humans are difficult terrain for SAR due to ubiquitous layover and occlusion issues accompanying buildings. This leads to limited visibility of objects (Soergel et al. 2003), which decreases the number of correspondences for stereo analysis and increases the size of areas that are hard to handle in InSAR processing, such as pure noise in shadow regions. The advanced German radar satellite TSX, launched June 15, 2007, offers a number of new perspectives and solutions for InSAR, particularly with its high-resolution imaging capability (1 m in high-resolution spotlight (HS) mode). Furthermore, the high range bandwidth of 150 MHz (or even 300 MHz) allows large baselines for highly precise DSM generation (Eineder et al. 2003) and the X-band presents new scattering properties such as PSI deformation measurement and monitoring (Crosetto et al. 2010).

This paper aims to extract a DEM of an urban area with intensive human settlement using TSX HS images.

## Test Site and Materials

The test site covers 4 km × 3 km (length and width) area on the European side of Istanbul, bordering the Bosphorus and the Marmara Sea with the elevation that ranges from sea level to 130 m. Figure 1 presents the high-resolution optical satellite image of the test site (a) and the frequency distribution of the terrain inclination (b).

The TSX project is a public-private partnership (PPP) between the German Ministry of Education and Science (BMBF), the German Aerospace Center (DLR) and Astrium, GmbH. Under the DLR contract, Astrium constructed the satellite, while DLR is responsible for the development of the ground segment, instrument calibration and scientific use of the satellite during its lifespan (DLR 2011). The system parameters and characteristics of the satellite are given in Eineder et al. (2003). The TSX collects data using three imaging modes: StripMap (SM), which is the most frequently applied mode (3 m resolution and long strips with 30 km swath widths); Spotlight (SL) (2 m resolution and 10 km × 10 km coverage); high-resolution Spotlight (1 m resolution and 5 km × 10 km coverage) and ScanSAR (16–30 m resolution and 100 km × 100 km coverage) (Roth 2003). By means of these modes, TSX images demonstrate a high potential for various scientific research activities such as object recognition (Wegner et al. 2010), wind and wave observation (Mendez et al. 2010), monitoring of water level changes in wetlands (Hong et al. 2010), traffic monitoring (Meyer et al. 2006), disaster monitoring (Martinis et al. 2009), forest monitoring (Breidenbach et al. 2010) and agriculture (Baghdadi et al. 2009; Anguela et al. 2010).

In this study, a suitable TSX HS mode image-pair is employed. In HS basic theory, the radar beam is focused similarly to a spotlight during the observation of a particular ground scene, so that the area of interest is illuminated for longer, increasing the synthetic aperture. The maximum azimuth steering angle range is  $\pm 0.75^\circ$  (Roth 2003) and single-

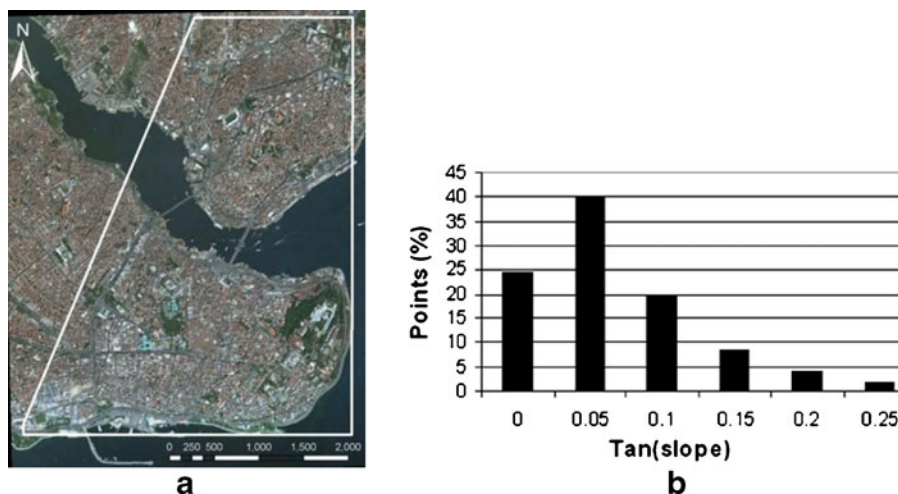


**Fig. 1** The test site (a) and the frequency distribution of the terrain inclination (b)

**Fig. 2** The TSX HS Istanbul SAR image-pair (a: image 1, b: image 2)



look complex data are available. Figure 2 and Table 1 illustrate the used image-pair and its characteristics.

### DEM Extraction Methodology

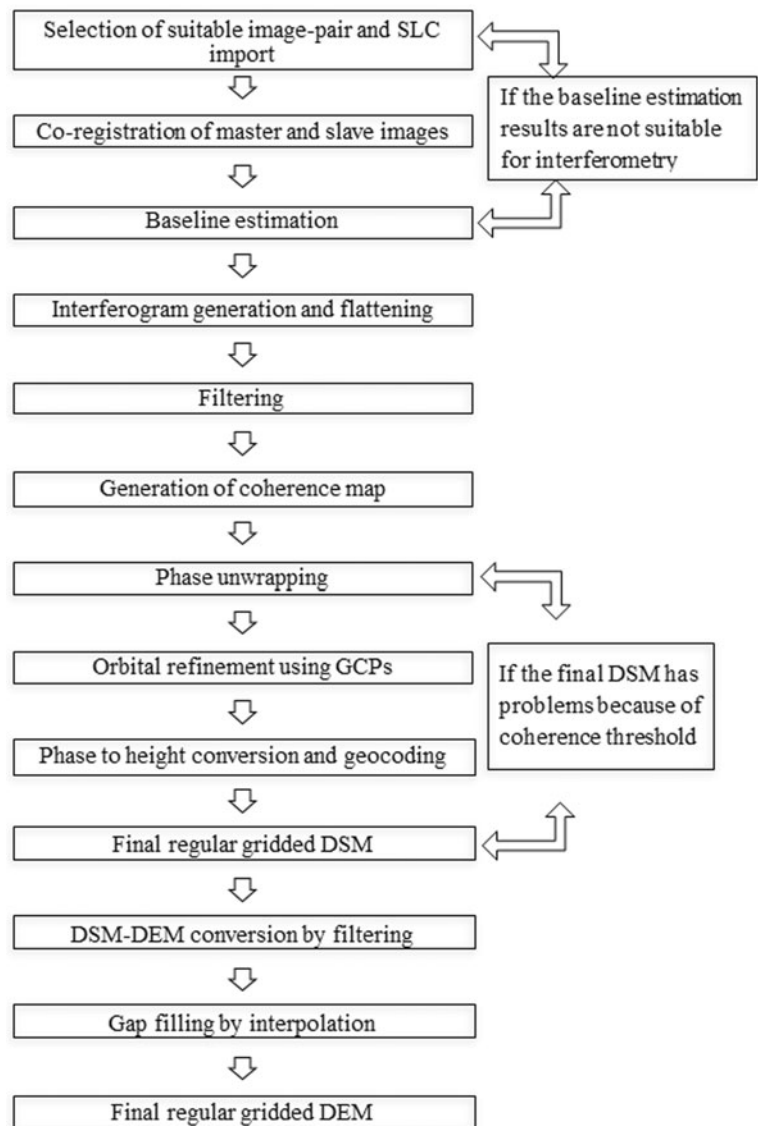
DEM extraction using SAR data consists of two main parts as DSM generation and DSM-DEM conversion. For DSM generation, interferometric processing steps are performed and extracted DSM is converted to DEM by filtering. Figure 3 shows the detailed flow chart of DEM extraction methodology in this study.

As can be seen in Fig. 3, DSM generation with interferometric processing consists of several complex processing steps including critical thresholds depending upon the quality and characteristics of the SAR data. At the beginning of interferometric processing, at least two concurrent SAR images of the area of interest are selected, providing the prerequisites for interferometry. To achieve reliable products, the imaging modes and the beams should be the same for the most coherent imaging geometry and the imaging periods should be similar to avoid atmospheric de-correlation due to seasonal variations. In co-registration and baseline estimation steps, one reference SAR

image is referred to as the master and a second image with similar acquisition geometry is referred to as the slave. The master and slave images should overlap to achieve sub-pixel accuracy in the slant range geometry. The co-registration of complex SAR images is accomplished in two parts: coarse co-registration (with an accuracy of 1–2 pixels) and fine co-registration (with an accuracy of 1/10 pixel) (Rabus et al. 2003; Li and Bethel 2008). At first, the location of each pixel in the slave image changes with respect to the master. Then, the amplitude and phase information of slave image is recalculated for each pixel by interpolation (Gens 1998) using bilinear or cubic convolution functions. The slave image resampling method is chosen based upon the type of terrain and the quality of the complex SAR images. At co-registration, the dependencies, range and azimuth grid positions and window numbers, orbit initialization, orbit accuracy and orbit interpolation values must be calibrated. Additionally, the window sizes, central positions of range and azimuth and cross-correlation threshold should be assigned. Eventually, the fine shift parameters should be determined, as well as the containing window sizes, range and azimuth window numbers, cross-correlation oversampling value, coherence oversampling value, reject and signal-to-noise ratio (SNR) threshold values. The number of tie

**Table 1** TSX HSSAR image pair characteristics

Characteristics	TSX HS image 1	TSX HS image 2
Sensor ID	SAR	SAR
Sensor mode	High resolution spotlight	High resolution spotlight
Beam	Spot_055	Spot_055
Start date(y-m-d)/time (h:m:s)	2008-05-05/15:57:33,985	2008-10-06/15:57:42,522
End date(y-m-d)/time (h:m:s)	2008-05-05/15:57:34,738	2008-10-06/15:57:43,262
Polarization mode	Single polarization	Single polarization
Polarization channel	HH	HH
Looking direction	Right looking	Right looking
Pass direction	Ascending pass	Ascending pass
Centre incidence angle	40.975°	41.089°
Scene center latitude	41.022°	41.025°
Scene center longitude	28.957°	28.940°
Resolution – slant range	0.588 m	0.588 m
Resolution – ground range	0.895 m	0.897 m
Resolution – azimuth	1.100 m	1.100 m
Length and width of scene	5 km×10 km	5 km×10 km

**Fig. 3** DEM extraction methodology

points (grid density), the width of the search window and the threshold for the correlation coefficient are extremely important in this step, as they influence the final results of the interferometric processing and the DSM accuracy. These values are usually determined by repeated tests.

The baseline estimation includes relevant parameters containing the normal baseline, the critical (maximum) baseline, the height of ambiguity ( $2\pi$  ambiguity height), the shifts in range and azimuth directions and the Doppler centroid difference. The normal baseline is the distance between two positions of SAR antenna in repeat-pass interferometry and perpendicular to the master and slave orbit, which is very significant for further interferometric processing. Initially, the normal baseline is computed based on the orbital parameters. In principle, a higher normal baseline is equivalent with higher DSM accuracy. However, if the magnitude of the normal baseline exceeds the threshold values, the noise affecting the interferogram increases and

the description of the topography and DSM generation become complicated. The critical normal baseline is given by the acquisition geometry and by the characteristics of the SAR sensor. An optimal value for the normal baseline maximizes the signal-to-noise ratio (Gatelli et al. 1994; Bamler 1997, 2006; Ferretti et al. 2007). Hence, the critical baseline should not be exceeded in any case. The  $2\pi$  ambiguity height represents the height difference of an interferometric fringe ( $2\pi$  cycle) and is inversely proportional to the normal baseline (Gatelli et al. 2009). An increase of this value obstructs the definition and delineation of small changes in height. The range and azimuth shifts are applied in the range and azimuth direction during the coarse master–slave co-registration. The difference between the master and slave Doppler centroids is called the Doppler centroid difference ( $f_D$ ). This value equals zero when the side look is  $90^\circ$  as the satellite travels in its flight direction (azimuth). Apart from that situation,  $f_D$  has a non-zero value that cannot exceed the pulse

repetition frequency (critical value). In this study, TSX HS image 1 was selected as the master and TSX HS image 2 was selected as the slave (see Fig. 2) and entire DSM generation processes were implemented in SARscape (version 4.3) module of ENVI software (version 4.8). The baseline estimation results between master and slave images are shown in Table 2.

### Interferogram Generation and Flattening

In single or double-pass (repeat-pass) interferometry, two SAR data sets are achieved simultaneously or at different times using different look angles for the same area of interest on the ground. These data sets contain the phase and magnitude of the backscattered radiation. The phase differences of the two co-registered complex-valued SAR data sets for the same area of interest are computed on a pixel-by-pixel base and an interferometric product is generated with the combination of them (Massonnet and Souyris 2008). This product is called an interferogram or a fringe map. Interferograms provide 3D visualization and topographic information can be derived from fringes, which are similar to contour lines. In addition to master and slave images, SPOT-5 HRS DSM and the precise orbital parameters were used for the interferogram generation in this study. The use of a DSM (an optional process) for interferogram generation allows the assignment of a reference cartographic system for the resulting DSM. During interferogram generation, the spectral shift and common Doppler bandwidth filtering are performed. The spectral shift is needed due to the range spectra shift for distributed targets caused by the variable SAR viewing angle, usually when the normal baseline has a high value (Ferretti et al. 2007). Doppler bandwidth filtering is required to compensate for different doppler squint angles, which produce shifted azimuthal spectra. In the case of SAR images acquired at large time interval, temporal de-correlation affects the quality of the interferometric phase, which is translated into noise. Noise reduction is performed by averaging the neighboring pixels of the complex interferogram, with the cost of lowering its spatial resolution. This process is called interferogram multi-looking (Manjunath 2008), computed based on the slant range and azimuth resolution and on the incidence angle at the center of the scene. A multi-looking factor of  $3 \times 3$  pixels was applied to TSX HS images

considering the grid spacing of final DSM. The produced interferogram from the TSX HS SAR image-pair is shown in Fig. 4.

After interferogram generation, several low-frequency components can be removed using interferogram flattening, the differential phase between the constant phase and the phase expected for flat or known topography. Therefore, this step consists of the removal of the interferometric phase component due to terrain topography. This process can be supported by a coarse DSM by transforming it into the master image slant range geometry. The synthetic fringes are generated from this DSM, otherwise the shape of the earth is assumed to be an ellipsoid and ellipsoidal height is used as a constant height. In this study, we used SPOT-5 HRS as a coarse DSM in the interferometric processing steps. The interferogram-flattening step is not a main step in DSM generation, but it is used to support the phase-unwrapping process. By interferogram flattening, it is observed that the numbers of fringes are reduced on the TSX HS interferogram.

### Filtering and Coherence Map Generation

Interferogram filters do not necessarily enhance or recover the radar signal, although a powerful filter that reduces noise caused by temporal or baseline related de-correlation changes the structure of the interferogram and improves fringe visibility. In this study, Goldstein, one of the most powerful adaptive radar interferogram filters (Goldstein and Werner 1998), was used for filtering. It is based on the concept of multiplication of the Fourier spectrum  $Z(u, v)$  of a small interferogram patch by its smoothed absolute value  $S\{|Z(u, v)|\}$  to the power of an exponent  $\alpha$ :

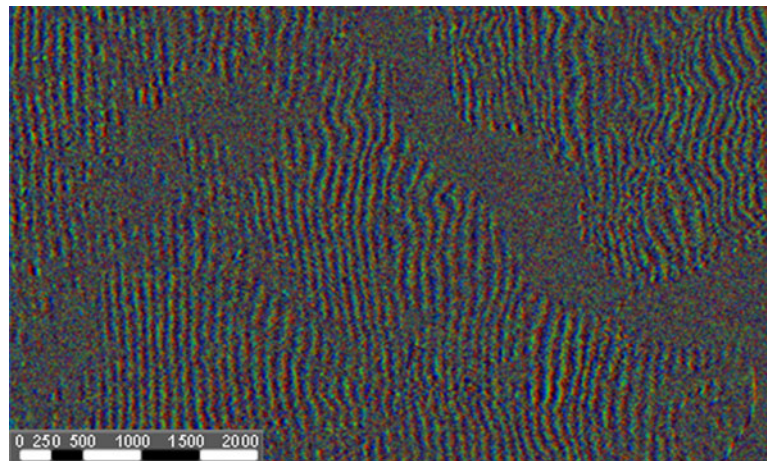
$$H(u, v) = S\{|Z(u, v)|\}^a \times Z(u, v) \tag{1}$$

where  $H(u, v)$  is the filter response (the spectrum of the filtered interferogram),  $S\{\}$  is a smoothing operator,  $u$  and  $v$  are spatial frequencies, and  $a$  is the filter parameter. Patches of the interferogram are defined and overlapped to prevent discontinuities at the boundaries. The interferogram is filtered in the spectral domain using a rectangular smoothing window of varying size. The filter parameter  $a$  is an arbitrarily chosen value between 0 (no filtering) and 1 (maximum filtering) and it has the largest impact on the filter performance. For  $a=0$ , the multiplication factor becomes 1 and no filtering occurs. However, for large values of  $a$ , the filtering is significant (Baran et al. 2003). The value of this parameter is chosen upon the correlation coefficient of the SAR images. If the correlation coefficient has a low value (less than 0.25) the filter is set to 0.2–0.5. In general, large smoothing windows are preferred for low correlation values (Goldstein and Werner 1998). Filtering of the interferogram generated from the TSX

**Table 2** Baseline estimation between the TSX HS master and slave images

Baseline estimation parameters	Values
Normal baseline (m)	136.21
Critical baseline (m)	15770.57
$2\pi$ ambiguity height (m)	45.95
Range Shift (pixels)	-2030.48
Azimuth Shift (pixels)	618.91
Doppler centroid difference (Hz) (Critical: 3514.78)	154.00

**Fig. 4** Interferogram of TSX HS image-pair



HS image-pair was performed using a filter parameter of 0.5 and a window of 128 pixels.

The interferometric coherence represents the stability of the backscattered SAR signal over an area of interest (Parcharidis et al. 2005) and should be defined as the ratio between coherent and incoherent synopsis. The coherence map is achieved by measuring the pixel-to-pixel SNR and exposes the quality and reliability of an interferogram. The equation relating SNR to coherence value ( $\gamma$ ) is;

$$SNR = \gamma^2 / (1 - \gamma^2) \tag{2}$$

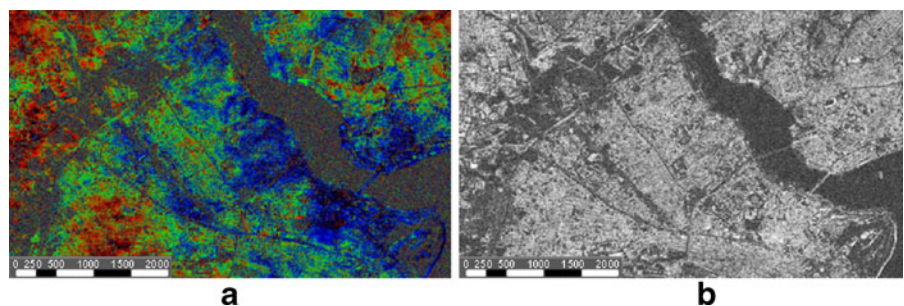
Coherence maps are acquired by iterating the sampled estimator given below for each pixel ( $k, h$ ) of the co-registered master ( $s_M$ ) and slave ( $s_S$ ) images, after compensating for the estimated local slopes ( $w_k, w_h$ ) (Guarnieri et al. 2003).

$$\gamma(k, h) = \frac{\sum_{ij} S_M(k-i, h-j) S_S^*(k-i, h-j) \exp(j(W_k i + W_h j))}{\sqrt{\sum_{ij} |S_M(k-i, h-j)|^2 |S_S(k-i, h-j)|^2}} \tag{3}$$

The coherence ranges between 0 (the phase is just noise) and 1 (a complete absence of noise), depending upon the noise of the SAR sensor, errors that occurred during the previous

interferometric steps (low accuracy co-registration), acquisition geometry (looking direction and incidence angle), systematic spatial de-correlation (due to terrain topography, slope and height differences), and temporal de-correlation between the master and slave image (Gatelli et al. 1994; Zhou et al. 2009). Coherence is a measure for describing the quality of the complex interferogram and, consequently, the generated DSM and the thematic information extracted related to ground objects according to the backscattering coefficient. The most important factor for coherence is the time interval between the master and slave images and changes in the imaged objects. A large acquisition interval significantly decreases the coherence based on changes in the objects caused by season, climate, etc., at the area of interest. According to Tran et al. (2007) an interferogram is considered to have good coherency if 80 % of the pixels have a coherence value better than 0.5. An interferogram with coherence values less than 0.2 cannot be unwrapped. Low coherence values usually occur in areas covered by water or dense vegetation, while high coherence values are characteristic of urban or rocky areas (Ferretti et al. 2007). For the generation of a coherence map, an interferogram or its filtered version are used. A filtered coherence map may be useful for higher coherence. Figure 5 shows the filtered interferogram of the TSX HS (a) and corresponding coherence map (b). The bright parts of the coherence map indicate areas with higher coherence, such as built-up or flat areas, and the dark parts indicate regions with lower coherence, such as sea, vegetation or forest.

**Fig. 5** Filtered interferogram (a) and the generated coherence map (b)



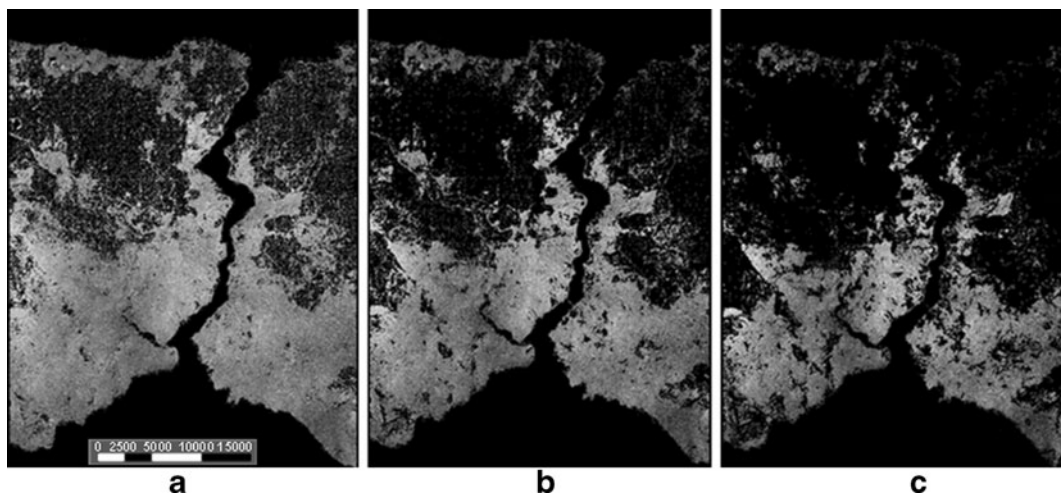


**Fig. 6** Effect of the coherence threshold in phase unwrapping (**a** = 0.35, **b** = 0.40, **c** = 0.5)

### Phase Unwrapping and Orbital Refinement

Phase unwrapping is the most complex step of interferometric processing and problems occur from aliasing errors due to phase noise caused by low coherence and under sampling because of locally high fringe rates (Reigber and Moreira 1997). To solve these problems, several algorithms, including, minimum cost flow and minimum least squares, have been developed. In this study, region growing algorithm (Reigber and Moreira 1997) with different decomposition levels was preferred for phase unwrapping. This method can be described in terms of two primitive operations: the translation operation, which adds or subtracts  $2\pi$  to all points in a region, and the connect operation, which merges two areas. Starting from a condition of maximum fragmentation where each point constitutes a region, these two operations are executed iteratively on the active areas until no additional joins can be done (Baldi 2003).

For excluding lower coherence areas, a threshold value should be defined during phase unwrapping. Nevertheless, by incorrect coherence threshold selection, several significant details may be lost and the operation may become illogical.

Figure 6 shows an example for three different coherence thresholds applied to the large part of Istanbul on a TSX Stripmap mode data and their effects on the results of phase unwrapping. The most of the lost details (black) appear in the intensive forest area at the north side of Fig. 6. As known, SAR imagery offers high coherence in open and built-up areas as our test site. Considering this fact and plotting the spatial profiles at the various parts of generated coherence map, we preferred to use 0.5 as the optimal coherence threshold. The resulting interferogram after phase unwrapping is shown in Fig. 7.

After phase unwrapping, orbital refinement is essential for DSM extraction (Tokunaga 1998). The relation between the phase difference and elevation is a function of the baseline and an accurate baseline is necessary for an accurate DSM. The baseline is initially estimated using the orbit information of the image header file and the orbital refinement improves the accuracy of the baseline value. In addition to refined orbits, phase compensation is calculated using ground control points (GCP), enabling the absolute phase calculation. GCPs should be determined precisely and located on flat, highly correlated areas (coherence map can be used for this process) and the residual orbital

**Fig. 7** Interferogram of the TSX HS after phase unwrapping

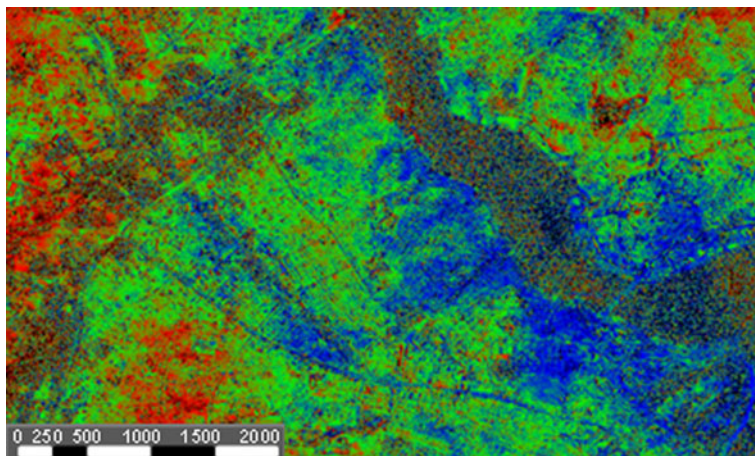
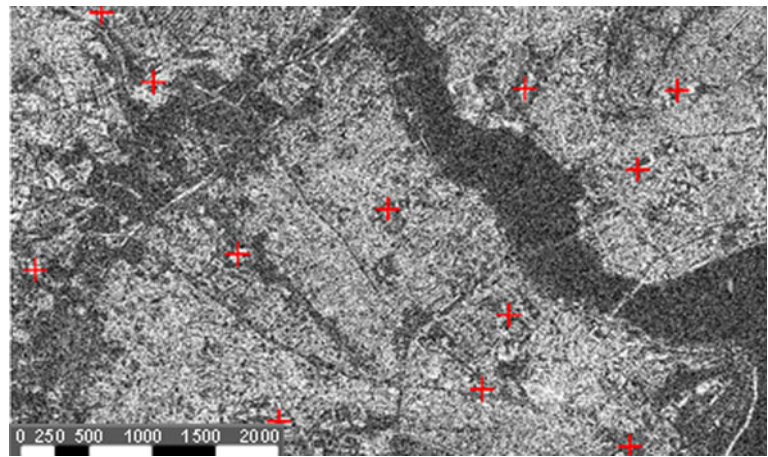


**Fig. 8** GCP distribution on coherence map



fringes, if present. The accuracy of the normal baseline determination should be within  $10^{-6}$ – $10^{-4}$  of the slant range value (Richards 2007). The baseline errors decrease the vertical accuracy of the DSM generated by interferometric means (Sowter 2003). In this study, 12 GCPs were used for the orbital refinement. Figure 8 shows the distribution of GCPs on the coherence map. To check the distribution and quality of GCPs, the Root Mean Square Error (RMSE) has to be examined in the modified phase-unwrapping header file. A maximum RMSE of 10 m indicates well-distributed and qualified GCPs. To provide requested accuracy, before the determination of a GCP in any location, plotting of a spatial profile on coherence map is recommended.

### Generation of Final DSM

At the last step of interferometric processing for DSM extraction, phase values should be converted to the height of each pixel in the interferogram. The conversion implies the re-projection from the SAR coordinate system of the complex images into a geocentric Cartesian system defined by X, Y planimetric coordinates and Z height (Crosetto and Perez Aragues 1999; Ferretti et al. 2007). The geocoding process of SAR images is different from optical imagery because SAR systems cause a non-linear compression

**Table 3** Used main parameters for interferometric processing

Processing Step	Parameter
Interferogram generation	Multilooking: 3×3 (Range×Azimuth)
Flatening	With SPOT-5 HRS
Filtering	Goldstein (2×2)
Phase unwrapping	Region growing algorithm; decomposition level: 3; coherence threshold: 0.5
Orbital refinement	12 GCPs (calculated RMSZ <10 m)
Phase to height conversion	3 m gridded DSM
Geocoding	Terrain geocoding, UTM WGS84 datum (central meridian=35°)

that cannot be corrected by using polynomials. The sensor and processor characteristics must be considered during the geometric correction. For this reason, the Range-Doppler approach is essential for geocoding SAR data. The Range Eq. (4) and the Doppler Eq. (5) must be performed for each image pixel:

$$R_s = S - P \tag{4}$$

$$f_D = \frac{2f_0(v_p - v_s)R_s}{c|R_s|} \tag{5}$$

Where  $R_s$  is the slant range,  $S$  and  $P$  are the spacecraft and backscatter element positions,  $v_p$  and  $v_s$  are the spacecraft and backscatter element velocities,  $f_0$  is the carrier frequency,  $c$  is the speed of light and  $f_D$  is the processed Doppler frequency. Instead of ellipsoidal geocoding, terrain geocoding was performed by means of a SPOT-5 HRS DSM. The coherence threshold, interpolation method, interpolation window size, mean window size and requested grid size should be carefully determined for more accurate conversion. Table 3 and Fig. 9 show the used main parameters at the interferometric processing and the extracted 3D DSM with an exaggeration factor of 3 for better interpretation respectively.

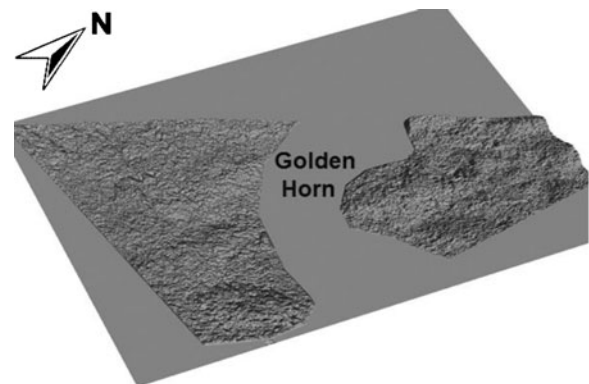


**Fig. 9** Extracted TSX HS DSM (exaggeration factor of 3)

**Table 4** Accuracy assessment of generated DEM according to prominent slope groups

DEM	RMSE $\Delta Z$ (m)		
	tan(slope)=0 (%40)	tan(slope)=0.05 (%25)	tan(slope)=0.10 (%20)
TSX HS (3 m)	7.09	7.65	8.21

DSM-DEM Conversion

In DSM-DEM conversion process, to obtain bare ground we preferred linear prediction algorithm for filtering considering dominant built-up coverage in the test site. We used RASCOR software (Day et al. 2013), developed by Dr. Karsten Jacobsen from Leibniz University Hannover, Institute of Photogrammetry and Geoinformation. The gaps, occurred at the locations of filtered non-terrain objects, were filled by ‘moving surface’ interpolation method, mostly preferred for the applications on flat terrain.

**Fig. 10** Reference DEM (a), TSX HS DEM (b), DIFFDEM (c) and coherence map of the TSX HS (d)

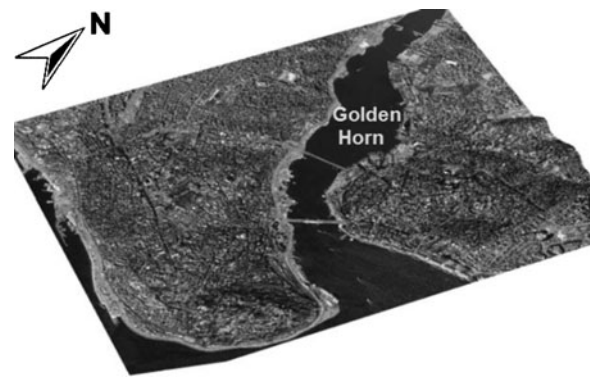
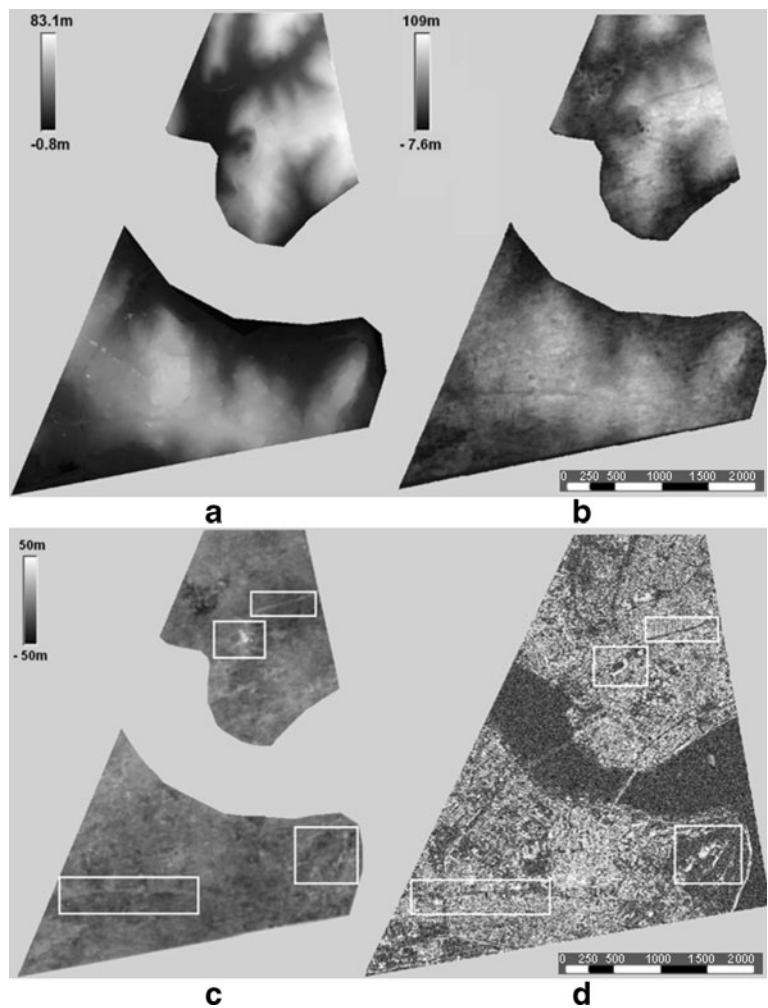


**Fig. 11** Perspective view display of IKONOS PAN and extracted TSX HS DEM

Vertical Accuracy Assessment of Extracted DEM

The vertical accuracy of a DEM, derived by InSAR technique, is affected by the following factors: value of the normal baseline between master and slave images (Bamler 2006), the accuracy of the interferometric phase computation, the accuracy of the geometry acquisition determination, the

accuracy of the removal of atmospheric errors, and phase-unwrapping results (Bamler 1997; Kyaruzi 2005; Ferretti et al. 2007; Richards 2007; Mohr and Boncori 2007). The accuracy was evaluated by comparing extracted DEM with a 3 m original gridded reference DEM, derived from 1:1000 scaled photogrammetric maps without having major distortions on the comparison area. In accuracy assessment, the extracted DEM was overlapped to the reference DEM by horizontal shifting and RMSE of height differences ( $\Delta Z$ ) was computed. For assessment process, BLUH (bundle block adjustment Leibniz University Hannover) (Jacobsen, unpublished data 2009) software was used. The results of the vertical accuracy assessment for prominent slope groups of the test area (see Fig. 1b) are shown in Table 4. Following Fig. 10 contains the reference DEM (a), the TSX HS DEM (b), the differential DEM (DIFFDEM) that illustrates pixel-based height differences between the TSX HS and reference DEM by height scale (c) and the coherence map of the TSX HS (d). Light and dark parts (white squares in Fig. 10c) indicate discordant areas that have low coherence (see Fig. 10d).

In SAR imagery, the accuracy is inversely proportional to terrain inclination where layover and shadows occur (Gens and Van Genderen 1996; Sefercik and Jacobsen 2007) and this provision was corrected by Table 4.

After determining the vertical accuracy, a perspective view display (Fig. 11) was generated to use in operational tasks (John and Cowen 1999) by draping extracted TSX HS DEM and high-resolution space-borne IKONOS panchromatic (PAN) image that has 1 m grid spacing.

## Conclusions

The high resolution interferometric DEM generation has become possible by InSAR technique using the data from space-borne SAR sensors such as TerraSAR-X (TSX) and Cosmo-SkyMed with improved ground resolution up to 1 m. Due to the intrinsic properties of used SAR signals and complex geometry of urban settlements, the interferometric DEM generation in urban areas is still complicated task.

In this paper, an attempt is presented to explore DEM extraction in urban areas by InSAR using TSX high resolution Spotlight (HS) images covering an urban part of Istanbul. The multi-step procedure interferometric processing for DSM generation has been performed with proposed approach using the assigned critical parameters and thresholds depending upon the quality and characteristics of the SAR data. The final DEM with 3 m grid spacing was generated after DSM-DEM conversion using optimal filtering algorithm and gap filling by interpolation. The quality of the resulting DEM has been analyzed by comparing a reference DEM, derived from 1:1000 scaled photogrammetric maps. The results reveal that the root mean square error of height differences between 7.09

and 8.11 m is achievable depending on the slope groups in study area. The results of further analyses show the correlation between low coherence and low vertical accuracy using the generated differential DEM. Overall; the obtained results verify that TSX HS images can be used for DEM extraction and various applications in urban areas which require 5–10 m vertical accuracy.

**Acknowledgments** Thanks are going to Turkish Scientific and Technical Research Institute (TÜBİTAK), Turkey, Romanian Space Agency, Romania, and DLR, Germany, for their supports to this research. And also we would like to thank Prof. Dr. Uwe Sörgel and Dr. Karsten Jacobsen from Leibniz University Hannover, Institute of Photogrammetry and Geoinformation.

## References

- Anguela, T. P., Zribi, M., Baghdadi, N., & Loumagne, C. (2010). Analysis of local variation of soil surface parameters with TerraSAR-X radar data over bare agricultural fields. *IEEE Transactions on Geoscience and Remote Sensing*, 48(2), 874–881.
- Baghdadi, N., Boyer, N., Todoroff, P., Hajj, M. E., & Begue, A. (2009). Potential of SAR sensors TerraSAR-X, ASAR/ENVISAT and PALSAR/ALOS for monitoring sugarcane crops on Reunion Island. *Remote Sensing of Environment*, 113(8), 1724–1738.
- Baldi, A. (2003). Phase unwrapping by region growing. *Applied Optics*, 42(14), 2498–2505.
- Bamler, R. (1997). Digital terrain models from radar interferometry. Photogrammetric Week, Stuttgart.
- Bamler, R. (2006). Radar interferometry for surface deformation assessment. Summer School Alpbach 2006: Monitoring of natural hazards from space, Alpbach.
- Baran, I., Stewart, M. K., Kampes, B. M., Perski, Z., & Lilly, P. (2003). A modification to the Goldstein radar interferogram filter. *IEEE Transactions on Geoscience and Remote Sensing*, 41(9), 2114–2118.
- Breidenbach, J., Ortiz, S. M., & Reich, M. (2010). Forest monitoring with TerraSAR-X: first results. *European Journal of Forest Research*, 129(5), 813–823.
- Christie, M., Tsoflias, G. P., Stockli, D. F., & Black, R. (2009). Assessing fault displacement and off-fault deformation in an extensional tectonic setting using 3-D ground-penetrating radar imaging. *Journal of Applied Geophysics*, 68(1), 9–16.
- COSMO-SkyMed. (2011). <http://www.cosmo-skymed.it/en/index.htm>.
- Crosetto, M. (2002). Calibration and validation of SAR interferometry for DEM generation. *ISPRS Journal of Photogrammetry & Remote Sensing*, 57(3), 213–227.
- Crosetto, M., & Perez Aragues, F. (1999). Radargrammetry and SAR interferometry for DEM generation: validation and data fusion. Proceedings of SAR Workshop: CEOS Committee on Earth Observation Satellites, Toulouse, ISBN: 9290926414, 26–29 October, Toulouse.
- Crosetto, M., Monserrat, O., Iglesias, R., & Crippa, B. (2010). Persistent scatterer interferometry: potential, limits and initial C- and X-band comparison. *Photogrammetric Engineering and Remote Sensing*, 76(9), 1061–1069.
- Day, D., Jacobsen, K., Passini, R., & Quillen, S. (2013). A study on accuracy and fidelity of terrain reconstruction after filtering DSMs produced by Aerial images and Airborne Lidar Surveys, ASPRS 2013, Baltimore Maryland USA, 24–28 March

- DLR. (2011). [http://www.dlr.de/eo/en/desktopdefault.aspx/tabid-5725/9296\\_read-15979/](http://www.dlr.de/eo/en/desktopdefault.aspx/tabid-5725/9296_read-15979/)
- Eineder, M., Runge, H., Boerner, E., Bamler, R., Adam, N., Schättler, B., Breit, H., & Suchandt, S. (2003). SAR interferometry with TerraSAR-X. Proceedings of the FRINGE Workshop (ESA SP-550), Frascati, 1–5 December 2003.
- Ferretti, A., MontiGuarnieri, A., Prati, C., Rocca, F., & Massonnet, D. (2007). InSAR principles: guidelines for SAR interferometry processing and interpretation, ESA Publications, Noordwijk, ISBN 92-9092-233-8, ISSN 1013-7076, 135 pages.
- Font, M., Amorese, D., & Lagarde, J. L. (2010). DEM and GIS analysis of the stream gradient index to evaluate effects of tectonics: the Normandy intraplate area (NW France). *Geomorphology*, 119(3–4), 172–180.
- Fraser, C. S. (2003). Prospects for mapping from high-resolution satellite imagery. *Asian Journal of Geoinformatics*, 4(1), 3–10.
- Gatelli, F., MontiGuarnieri, A., Parizzi, F., Pasquali, P., Prati, C., & Rocca, F. (1994). The wavenumber shift in SAR interferometry. *IEEE Transactions on Geoscience and Remote Sensing*, 32(4), 855–865.
- Gatelli, D., Kucherenko, S., Ratto, M., & Tarantola, S. (2009). Calculating first-order sensitivity measures: a benchmark of some recent methodologies. *Reliability Engineering & System Safety*, 94(4), 1212–1219.
- Gens, R. (1998). Quality assessment of SAR interferometric data, Hannover, University of Hannover PhD Thesis, 141p.
- Gens, R., & Van Genderen, J. L. (1996). SAR interferometry-issues, techniques, applications. *International Journal of Remote Sensing*, 17(10), 1803–1835.
- Goldstein, R. M., & Werner, C. L. (1998). Radar interferogram filtering for geophysical applications. *Geophysical Research Letters*, 25(21), 4035–4038.
- Guarnieri, A. M., Guccione, P., Pasquali, P., & Desnos, Y. L. (2003). Multi-mode ENVISAT ASAR interferometry: techniques and preliminary results. *IEE Proceedings: Radar, Sonar and Navigation*, 150(3), 193–200. doi:10.1049/ip-rsn:20030516.
- Guindon, B., Goodenough, D. G., & Teillet, P. M. (1982). The role of digital terrain models in the remote sensing of forests. *Canadian Journal of Remote Sensing*, 8(1), 4–16.
- Hensley, S., Munjy, R., & Rosen, P. (2001). Interferometric synthetic aperture radar (IFSAR), digital elevation model technologies and applications. In: D. F. Manue (Eds.), *The DEM user's manual*, Maryland, pp. 142–207.
- Herland, E. A. (1996). Operational use of SAR interferometry for DEM generation and land use mapping, ERS SAR interferometry. In: T. D. Guyenne, D. Danesy (Eds.), Proceedings of the Fringe 96 Workshop, pp 203, Zurich.
- Hong, S., Wdowinski, S., & Kim, S. (2010). Evaluation of TerraSAR-X observations for wetland InSAR application. *IEEE Transactions on Geoscience and Remote Sensing*, 48(2), 864–873.
- Jacobsen, K. (2009). *Manual of bundle block adjustment Leibniz University Hannover*. Hannover: Institute of Photogrammetry and Geoinformation.
- Jain, M. K., & Singh, V. P. (2005). DEM-based modelling of surface runoff using diffusion wave equation. *Journal of Hydrology*, 302(1–4), 107–126.
- Jenson, S. K., & Domingue, J. O. (1988). Extracting topographic structure from digital elevation data for geographic information system analysis. *Photogrammetric Engineering and Remote Sensing*, 54(11), 1593–1600.
- John, M. S., & Cowen, M. B. (1999). Use of perspective view displays for operational tasks, Technical Report, CA 92152–5001, March 1999, SSC San Diego, USA.
- Kyaruzi, J. K. (2005). Quality assessment of DEM from radargrammetry data - Quality assessment from the user perspective, Enschede, International Institute for Geoinformation Science and Earth Observation Msc Thesis., 69p.
- Li, F.K., & Bethel, J. (2008). Image coregistration in SAR interferometry. *The International Archives of Photogrammetry, Remote Sensing and Spatial Information Sciences*, ISPRS Congress, vol. XXXVII, part B1/I, (pp. 433–438). Beijing, China.
- Liu, H., Jezek, K. C., & Li, B. (1999). Development of an Antarctic digital elevation model by integrating cartographic and remotely sensed data: geographic information system based approach. *Journal of Geophysical Research*, 104(B10), 23199–23213.
- López-Quiroz, P., Doin, M., Tupin, F., Briole, P., & Nicolas, J. (2009). Time series analysis of Mexico City subsidence constrained by radar interferometry. *Journal of Applied Geophysics*, 69(1), 1–15.
- Manjunath, D. (2008). Earthquake interaction along the Sultandagi-Akshir fault based on InSAR and Coulomb stress modeling. Columbia. University of Missouri PhD Thesis, 65p.
- Martinis, S., Twele, A., & Voigt, S. (2009). Towards operational near real-time flood detection using a split-based automatic thresholding procedure on high resolution TerraSAR-X data. *Natural Hazards and Earth System Sciences*, 9, 303–314.
- Massonnet, D., & Souyris, J. C. (2008). Imaging with synthetic aperture radar, EPEL Press, CRC Press, ISBN: 978-2-940222-15-5 (EPEL Press), ISBN 978-0-8493-8239-0 (CRC Press), 280 pages.
- Mendez, G., Lehner, S., Torres, F., Li, X., & Brusch, S. (2010). Wind and wave observations off the south Pacific Coast of Mexico using TerraSAR-X imagery. *International Journal of Remote Sensing*, 31(17–18), 4933–4955.
- Meyer, F., Hinz, S., Laika, A., Wehling, D., & Bamler, R. (2006). Performance analysis of the TerraSAR-X traffic monitoring concept. *ISPRS Journal of Photogrammetry & Remote Sensing*, 61(3–4), 225–242.
- Mohr, J. J., & Boncori, J. P. M. (2007). A framework for error prediction in interferometric SAR. Proceedings of the ENVISAT Symposium, 23–27 April, Montreux.
- Parcharidis, I., Fomelis, M., Lekkas, E., & Segou, M. (2005). Implication of secondary geodynamic phenomena on co-seismic interferometric coherence. Advances in SAR Interferometry From ENVISAT and ERS Missions, ESA ESRIN, 28 November–2 December, Frascati.
- Rabus, B., Eineder, M., Roth, A., & Bamler, R. (2003). The shuttle radar topography mission – a new class of digital elevation models acquired by spaceborne radar. *ISPRS Journal of Photogrammetry & Remote Sensing*, 57(4), 241–262.
- Ranganath, R. N., Jayaraman, V., & Roy, P. S. (2007). Remote sensing applications: an overview. *Current Science*, 93(12), 1747–1766.
- Reigber, A., & Moreira, J. (1997). Phase unwrapping by fusion of local and global methods. geoscience and remote sensing., Proceedings of IGARSS'97, Singapore, 3–8 August 1997, pp. 869–871.
- Richards, M. (2007). A beginner's guide to interferometric SAR concepts and signal processing. *IEEE A & E Systems Magazine*, 22(9), 5–29.
- Rosen, P. A., Hensley, S., & Joughin, I. R. (2000). Synthetic aperture radar interferometry. *Proceedings of the IEEE*, 88(3), 333–382.
- Roth, A. (2003). TerraSAR-X: A new perspective for scientific use of high resolution spaceborne SAR data. 2nd GRSS/ISPRS Joint Workshop on Data Fusion and Remote Sensing over Urban Areas, Berlin, 22–23 May 2003.
- Schmidt, F., & Persson, A. (2003). Comparison of DEM data capture and topographic wetness indices. *Precision Agriculture*, 4(2), 179–192.
- Sefercik, U. G., & Alkan, M. (2009). Advanced analysis of differences between C and X bands using SRTM data for mountainous topography. *Journal of the Indian Society of Remote Sensing*, 37, 335–349.
- Sefercik, U. G., & Jacobsen, K. (2006). Analysis of SRTM height models. Fifth International Symposium Turkish-German Geodetic Days, Berlin, 28–31 March 2006.
- Sefercik, U. G., & Jacobsen, K. (2007). Quality assessment of INSAR digital elevation models. 27th EARSeL Symposium: Geoinformation in Europe, Bolzano, 4–7 June 2007.

- Soergel, U., Thoennessen, U., & Stilla, U. (2003). Visibility analysis of man-made objects in SAR image. IEEE/ISPRS Joint Workshop on Remote Sensing and Data Fusion Over Urban Areas, pp. 120–124.
- Sowter, A. (2003). Phase ambiguity determination for the positioning of interferometric SAR data. *Photogrammetric Record*, 18(104), 308–324.
- Stereńczak, K., & Kozak, J. (2011). Evaluation of digital terrain models generated in forest conditions from airborne laser scanning data acquired in two seasons. *Scandinavian Journal of Forest Research*, 26(4), 374–384.
- Thompson, J. A., Bell, J. C., & Butler, C. A. (2001). Digital elevation model resolution: effects on terrain attribute calculation and quantitative soil-landscape modeling. *Geoderma*, 100(1–2), 67–89.
- Tokunaga, K. (1998). DEM generation using JERS-1 SAR interferometry. ISPRS commission IV symposium on GIS between vision and applications. 32(4), (pp. 625–628). 7–10 September, Stuttgart, Germany.
- Toutin, T., & Gray, L. (2000). State-of-the-art of elevation extraction from satellite SAR data. *ISPRS Journal of Photogrammetry & Remote Sensing*, 55(1), 13–33.
- Tran, V. A., Masumoto, S., Raghavan, V., & Shiono, K. (2007). Accuracy of low relief topographical map derived from JERS-1 SAR interferometry in Hanoi. *Journal of Geosciences*, 50(8), 93–106.
- Wegmüller, U., Santoro, M., Werner, C., Strozzi, T., Wiesmann, A., & Lengert, W. (2009). DEM generation using ERS–ENVISAT interferometry. *Journal of Applied Geophysics*, 69, 51–58.
- Wegner, J.D., Ziehn, J.R., Soergel, U. (2010). Building detection in urban areas from combined optical and InSAR data exploiting context. EARSeL Workshop, Gent.
- Wolock, D. M., & Price, C. V. (1994). Effects of digital elevation model map scale and data resolution on a topography-based watershed model. *Water Resources Research*, 30(11), 3041–3052.
- Yastikli, N., Kocak, G., & Büyüksalih, G. (2006). Accuracy and morphological analyses of GTOPO30 and SRTM X – C band DEM in the test area Istanbul. Proceeding of ISPRS Ankara Workshop on Topographic Mapping From Space With Special Emphasis on Small Satellites, Ankara, 14–16 February 2006.
- Zhou, X., Chang, N. B., & Li, S. (2009). Applications of SAR interferometry in Earth and environmental science research, *Sensors* ISSN 1424-8220, (9), doi:10.3390/s90301876.